JGR Oceans

Key Points:

- A new satellite altimetry data set allows the detection of mesoscale eddies in the ice-covered Southern Ocean
- Eddy generation and strength are primarily impacted by sea ice concentration and the background circulation
- While the eddy strength is damped under high sea-ice concentration, the northern edge of the sea-ice region is a hotspot of large eddies

Correspondence to:

M. Auger,
matthis.auger@utas.edu.au

Southern Ocean Ice-Covered Eddy Properties From Satellite Altimetry

Matthis Auger[1,2,3] , **Jean-Baptiste Sallée[3]** , **Andrew F. Thompson[4]** , **Etienne Pauthenet[3,5]**, and **Pierre Prandi[6]**

[1]Insitute for Marine and Antarctic Studies, University of Tasmania, Hobart, Australia, [2]The Australian Centre for Excellence in Antarctic Science, University of Tasmania, Hobart, TAS, Australia, [3]CNRS, LOCEAN, Sorbonne Université, Paris, France, [4]Environmental Sciences and Engineering, California Institute of Technology, Pasadena, CA, USA, [5]Laboratoire d'Océanographie Physique et Spatiale (LOPS), Ifremer, CNRS, IRD, IUEM, Université de Brest, Plouzané, France, [6]Collecte Localisation Satellite, Toulouse, France

Abstract We investigate statistical properties of surface currents as well as coherent mesoscale eddies in the seasonally ice-covered Southern Ocean. Based on a recent regional Sea Level Anomaly satellite altimetry data set, we compute Eddy Kinetic Energy (EKE) and detect mesoscale eddies. EKE is about one order of magnitude higher in the northern sector of the subpolar basin and over the continental slope, as compared to the middle of the subpolar gyres. An eddy detection methodology reveals that eddies are distributed evenly in the subpolar Southern Ocean, and their amplitude follows the spatial pattern of EKE. In addition to regional circulation variations, sea ice concentration arises as an important driver of eddy properties. Eddies have low amplitude and density in the pack ice, in particular in the middle of the gyres where the background circulation is unfavorable for instabilities. In contrast, the northern part of the Marginal Ice Zone is favorable for mesoscale eddies, especially cyclonic. There, eddies are stronger and their density is higher than in any other region of the ice-covered or ice-free subpolar Southern Ocean. This region is expected to be a site of frontogenesis due to sea ice melt and upwelling generated from interactions between the wind and the sea ice. While many mesoscale eddies will fall below detection level due to the small Rossby radius at high latitudes, these results contribute to understanding the interactions between mesoscale eddies, sea ice, and the background circulation in the subpolar region.

Plain Language Summary Ocean eddies are spatially coherent vortices, ubiquitous in the global oceans, and are central structures contributing to shaping the global ocean circulation. In the Southern Ocean, they have been shown to play a potentially important role in the cross-front transport of heat and nutrients at mid and high latitudes. Recent improvements in satellite altimetry capabilities in the ice-covered regions allow for a first description of mesoscale eddies in the ice-covered Southern Ocean, and the investigation of their interactions with sea ice. The location of the detected eddies is consistent with the main large-scale circulation features. In addition to the background circulation, the sea ice cover has a strong impact on the size of eddies. While weaker eddies are found in the highly concentrated sea ice areas, the marginal ice zone seems to be a region with enhanced eddy activity, with more and stronger eddies detected.

1. Introduction

The oceanic circulation is a turbulent system dominated by mesoscale instabilities: in the global oceans, eddies are 10 times more energetic than the mean currents (Morrow & Le Traon, 2012). Mesoscale eddies are coherent vortices with spatial scales ranging from tens to hundreds of km, and with lifetimes from several weeks to several months (Chelton et al., 2011). These structures are essential for ocean dynamics, as they can induce mass and tracer transport through the so-called "bolus" velocity and also by trapping and translating water properties in their core (Chelton et al., 2011; McWilliams, 1985; Morrow & Le Traon, 2012). Eddies also increase diffusion of tracers through their stirring of the ocean (Garrett, 1983; Gent et al., 1995), and convert potential energy into kinetic energy through baroclinic instability, while transferring this energy across various scales (Stammer, 1998; Visbeck et al., 1997).

Eddies are detectable from surface topography maps derived from satellite altimetry. From the 2000s, high-resolution Sea Surface Height (SSH) products (Ducet et al., 2000) showed the ubiquity of mesoscale eddies in the global oceans. Chelton (2013) described eddy characteristics in the global ocean by applying eddy

detection and tracking algorithms to a high-resolution Sea Surface Height data set. Most of the eddies they observed were nonlinear, defined by a rotation speed that exceeds the translation speed (Chelton et al., 2011). The scale of eddies is intimately linked to the first baroclinic Rossby radius of deformation (Chelton et al., 1998), which varies from larger scales ($\simeq$250 km) at the equator to smaller scales (up to $\simeq$5 km and potentially less) at high latitudes (Chelton, 2013). Chelton (2013) also mapped the mean radius, translation, and rotation speed of the eddies, allowing for a better representation of mesoscale eddies and their disparities between the various oceanic basins of the globe.

Ocean eddies are particularly important in the Southern Ocean circulation, as they provide the dominant mechanisms for meridional heat and volume transport across the upper-ocean Antarctic Circumpolar Current (ACC) (Jayne & Marotzke, 2002). Eddies are also central for setting the ACC momentum balance (Gille, 1997; S. Rintoul et al., 2001; Ivchenko et al., 2008), and the structure of the Southern Ocean meridional overturning circulation (Speer et al., 2000; G. J. Marshall, 2003; J. Marshall & Radko, 2003; Ivchenko et al., 2008). In the context of a changing climate, Southern Ocean eddies are thought to be important in shaping the response of the ACC and the response of the overturning circulation to changes in westerly winds (Farneti et al., 2010; Dufour et al., 2012; Patara et al., 2016; Bishop et al., 2016; Gent, 2016; S. R. Rintoul, 2018).

In contrast to the ACC region, Southern Ocean eddies in the subpolar gyres (south of the ACC) are poorly described and understood because of the presence of sea ice that limits direct observations. However, we know that eddies remain an essential component of the circulation and transport of water masses. For instance, Nøst et al. (2011) and Thompson et al. (2014) found a fingerprint of eddy transport across the slope of the Antarctic continental shelf and suggested an important eddy contribution to the Antarctic overturning circulation through cross-slope transport of the warm intermediate layers. Later, Stewart and Thompson (2015) confirmed from an eddy-resolving model of the Antarctic Slope Front (ASF) that eddies are efficient for the shoreward transport of relatively warm Circumpolar Deep Water (CDW) along density surfaces. This onshore transport is enhanced by bathymetric features such as the coastal troughs in the continental shelf of the Bellingshausen sector (Nakayama et al., 2014), or at bottom water formation sites (Stewart & Thompson, 2015). Eddy stirring is also an important process in transferring heat toward the shelf (Palóczy et al., 2018; Stewart et al., 2018). Eddies also impact the intensity of the Antarctic Slope Current (Stewart et al., 2019).

While models highlight a potentially important role for eddies in the subpolar region of the Southern Ocean, mesoscale activity remains largely unknown in this region from large-scale observations (Vernet et al., 2019). Signatures of mesoscale eddies in ice-covered regions have been observed from moorings (Meneghello et al., 2020), ice-tethered profilers (Timmermans et al., 2008; Zhao et al., 2014, 2016) profiling glider sections (Thompson et al., 2014), or satellite-based Synthetic Aperture Radar (SAR) images (Kozlov et al., 2019). However, none of these methods provide wide spatio-temporal coverage to robustly describe eddy characteristics, a prerequisite towards investigating their influence on the large-scale circulation. In the Arctic basin, Meneghello et al. (2020) combined observations and high-resolution modeling to establish the seasonality of mesoscale activity as a function of depth and sea ice cover. Surface eddies were found to be highly damped by sea ice, while eddies in the halocline had more uniform energy levels throughout the year. These halocline eddies are predominantly cold-core anticyclonic eddies and are found in higher Sea Ice Concentration (SIC) areas, close to the topographic margins and boundaries of the Beaufort Gyre (Zhao et al., 2014, 2016). In the subpolar Southern Ocean, large-scale description of mesoscale eddies and their interaction with sea ice are still entirely lacking.

In this paper, we investigate mesoscale eddy properties by leveraging a new satellite altimeter product (Auger, Prandi, & Sallée, 2022). One important challenge in analyzing this data product is the decreasing Rossby Radius at high latitude, which is only 10–20 km in the subpolar gyres, and as small as a few km over the continental shelf. However, eddies larger than the Rossby radius are expected to exist due to the inverse energy cascade, especially in the high latitudes oceans where the beta effect is weak (Larichev & Held, 1995). In the Arctic, observations of eddies larger than the Rossby radius have been reported (Kubryakov et al., 2021; Sévigny et al., 2015; Watanabe, 2011).

Thus, even with the existing gridded products, which have a grid resolution of 25 km at best (Auger, Prandi, & Sallée, 2022), an exhaustive description of eddy activity remains out of reach. Still, eddy detection remains possible in regions with a low Rossby radius, such as the Mediterranean Sea (Escudier et al., 2016). In this paper, we consider products that sample eddies, even if aliased in some regions, to propose a first description of regional eddy characteristics and variability in the subpolar sector of the Southern Ocean. We apply an eddy detection and
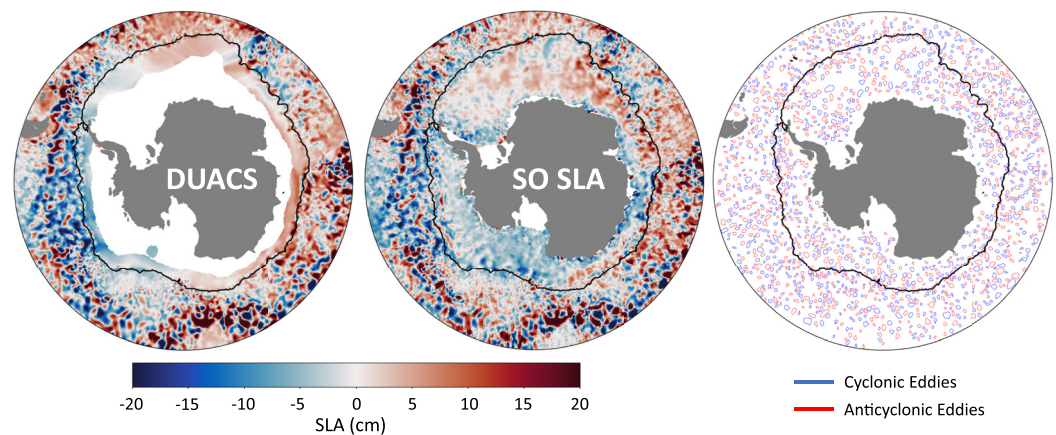
Figure 1. Sea level anomaly datasets and eddy detection (a) Sea level anomaly snapshot south of 50°S from DUACS product (Taburet et al., 2019). (b) Sea level anomaly snapshot from Auger, Prandi, and Sallée (2022) regional Southern Ocean data set. (c) Eddies detected south of 50°S from (Auger, Prandi, & Sallée, 2022) data set. Cyclonic eddies are represented in blue, anticyclonic eddies are represented in red. The black contour is the sea ice 3% sea ice concentration contour. All snapshots are taken at date 2017/09/01.

tracking method, described in Section 2, and investigate eddy characteristics and how they relate to sea ice cover and the dynamical regimes of the subpolar gyres in Section 3. We first describe the spatial variability of the EKE from the daily Sea Level Anomaly (SLA). We then evaluate the impact of sea ice concentration and ocean depth (as a proxy for shelf, slope, and abyssal plains) on the presence and strength of the detected eddies. Lastly, we focus on the Marginal Ice Zone which stands out as a region with enhanced eddy activity. We discuss the implication and limitations of our approach in Section 4 and provide a brief conclusion in Section 5.

2. Data and Methods

2.1. Data Sets

2.1.1. SLA Product

The regional SLA product used in this paper is presented in detail in Auger, Prandi, and Sallée (2022), and is available on SEANOE with the https://doi.org/10.17882/81032 (Auger et al., 2021). The data product consists of 7 years (2013–2019) of daily SLA and associated geostrophic current anomalies on a 25 km EASE2 grid (Brodzik et al., 2014). The product is based on the processing and mapping of observations from three satellites: AltiKa and Sentinel-3A in the open and ice-covered oceans, and Cryosat-2 in the ice-covered regions. Data set validation and error estimation are described in Auger, Prandi, and Sallée (2022). Figures 1a and 1b shows the gain of spatial coverage in the ice-covered Southern Ocean from the commonly used, global DUACS data set (Taburet et al., 2019) and the regional Auger, Prandi, and Sallée (2022) data set.

2.1.2. Other Data Sets

The Mean Dynamic Topography (MDT) represents the mean surface of the ocean relative to the geoid. To compute the Absolute Dynamic Topography (ADT), needed to track eddies, we add the time-mean MDT from Armitage et al. (2018) to the daily evolving SLA from Auger, Prandi, and Sallée (2022).

We also use satellite-based sea ice observations: Sea Ice Concentration (Meier et al., 2017; Peng et al., 2013) and Sea Ice Drift velocity from the National Centers for Environmental Information (Tschudi et al., 2016).

The bathymetric data used in this study comes from the R-Topo2 data set (Schaffer et al., 2019).

2.2. Methods

2.2.1. Eddy Detection and Tracking

Eddy detection and tracking methods are derived from Mason et al. (2014). The method is based on the analysis of ADT in which eddies are identified as small-scale closed contours. The first step is to remove the large-scale

pattern by applying a 600 km high-pass Gaussian filter to the ADT field. A high-pass filter with a cutoff of several hundreds of km is needed to remove the large scale signal from the data set (Mason et al., 2014; Pegliasco et al., 2021). The spatial scale of 600 km is arbitrarily chosen here, but the results are not sensitive to this scale as long as the filter is sufficiently large so as not to remove mesoscale features. Then, eddies are identified by searching for closed contours. Once a closed contour is found, several tests are performed, as described below, to ensure that the feature corresponds to a mesoscale eddy.

The series of tests applied to detect eddies from the ensemble of SLA closed contours are listed in Mason et al. (2014), and are presented here for the convenience of the reader. First, the contour circularity is checked by computing the ratio between the surface area of the identified eddy and the surface area of its circular approximation; this ratio must be larger than 0.7. Additionally, an eddy must contain at least eight pixels in the grid and have an ADT anomaly greater than 1 cm. The eddy must also contain only SLA pixels with values lower than the closed contour for a cyclone, and higher than the closed contour for an anticyclone, while containing only one local maximum or minimum of SLA. When a closed contour passes all these tests, it is considered an eddy. It is then possible to compute its properties, which include its rotation speed, radius, center, and amplitude. The amplitude is computed as the height of the trough or the bump in ADT associated with each eddy. Both cyclonic and anticyclonic eddies are detected in all the ice-covered Southern Ocean, as illustrated in Figure 1c. Once eddies are detected for each time step, it is possible to track their trajectories.

The tracking process consists in drawing ellipses of 150 km radius around eddies and determining the candidates, that are eddies detected the day after, that fall into this ellipse (Chelton et al., 2011). When there are multiple candidates, the couple is determined by minimizing S: a dimensionless parameter computed from the distance, radius differences, and amplitude differences between the eddies and their candidates. As in Mason et al. (2014), S is defined for each eddy at the date k and candidates $k + 1$ as:

$$S_{k,k+1} = \sqrt{\left(\frac{\Delta d}{d_0}\right)^2 + \left(\frac{\Delta a}{a_0}\right)^2 + \left(\frac{\Delta A}{A_0}\right)^2}, \tag{1}$$

where Δd is the distance between the eddy at the date k and the candidate at the date $k + 1$, Δa and ΔA are the difference in area and eddy amplitude, respectively, between the eddy and the candidate eddy.

In this study, we only consider eddies that have been tracked for 10 days or more. This allows the removal of more than 30,000 eddy identifications over the seven years in the subpolar Southern Ocean, to remove potential noise, and to concentrate on eddies that may have a stronger influence on the subpolar Southern Ocean water masses and circulation. The tracking is only used as a way to remove potential noise. In this study, we do not investigate the lifetime or trajectories of the eddies. Indeed, the small size of the eddies makes them difficult to track for long time periods, as some positions of the eddies may be missed during their lifetime due to sampling gaps.

2.2.2. Computation of the Eddy Kinetic Energy

The EKE over the Southern Ocean, south of 50°S, is computed from Auger, Prandi, and Sallée (2022) SLA and geostrophic current anomalies products following,

$$EKE = \frac{1}{2}\left(u'^2 + v'^2\right), \tag{2}$$

with u' and v' respectively the anomalies of zonal and meridional geostrophic current from the data set from the 2013–2019 mean state.

2.2.3. Ekman Pumping Velocities

In this paper, we investigate the impact of wind and ice stress on the Ekman pumping at the surface of the ocean. We follow the method outlined in Auger, Prandi, and Sallée (2022) to compute the combined effect of wind and sea ice on the surface stress. In regions with sea ice cover, part of the wind-induced surface stress is suppressed by the sea ice, while the ocean is subject to ice-induced surface stress (Martin et al., 2016; Tsamados et al., 2014). The total stress at the surface of the ocean $\vec{\tau}_{ocn}$, is given by:

$$\vec{\tau}_{ocn} = (1 - A_i)\vec{\tau}_{ao} + A_i\vec{\tau}_{iw}, \tag{3}$$

where $\vec{\tau}_{ao}$ and $\vec{\tau}_{iw}$ represent the wind and ice stresses respectively, and A_i the sea ice concentration.

The wind stress $\vec{\tau}_{ao}$ is computed as:

$$\vec{\tau}_{ao} = \rho_a C_{dao} |\vec{u}_a - \vec{u}_w| (\vec{u}_a - \vec{u}_w),\tag{4}$$

while the ice stress $\vec{\tau_{iw}}$ is computed as:

$$\vec{\tau}_{iw} = \rho_w C_{dw} |\vec{u}_i - \vec{u}_w| (\vec{u}_i - \vec{u}_w).\tag{5}$$

The total ocean stress depends on the sea ice concentration A_i taken from NCEI (National Centers for Environmental Information; https://doi.org/10.7265/N59P2ZTG) as the sea ice velocity $\vec{u}_i$ (https://doi.org/10.5067/O57VAIT2AYYY). Both datasets are mapped on 25 km grids. Here, ρ_a and C_{dao} are the air density and air-ocean drag coefficients, respectively, and are taken from Tsamados et al. (2014). The ocean density is $\rho_w = 1,028$ kg m^{-3}, and the ocean-ice drag coefficient is $C_{dw} = 5.50 \times 10^{-3}$, as used in Garabato et al. (2019). Ocean velocities $\vec{u}_w$ are obtained as in Auger, Sallée, et al. (2022) from Auger, Prandi, and Sallée (2022) data set. Wind velocities $\vec{u}_a$ are estimated from ECMWF (European Centre for Medium-Range Weather Forecasts) ERA5 monthly mean output (https://doi.org/10.24381/cds.f17050d7) on 0.25°, linearly interpolated on a 25 km grid.

Finally, we compute the Ekman pumping w_e as in Ramadhan et al. (2022):

$$w_e = \nabla \times \left(\frac{\vec{\tau_{ocn}}}{\rho_w f} \right).\tag{6}$$

where f is the Coriolis parameter.

2.2.4. Definition of Sea Ice Regions

The sea ice cover can be decomposed into various sectors corresponding to different ranges of sea ice concentrations. At high concentrations, typically above 70%, the drifting sea ice cover is referred to as pack ice. Lower concentrations, but above 10%, are commonly referred to as the Marginal Ice Zone (MIZ), which itself can be decomposed in a southern part of MIZ called "open ice" for concentrations between 40% and 70%, and a northern part of MIZ called "very open ice" for concentrations between 10% and 40%. In the present paper, we adopt these terms and definitions in agreement with the World Meteorological Organization sea ice nomenclature (Ice, 2009). We refer to the 10%–40% sea-concentration sector as n-MIZ and the 40%–70% sea-concentration sector as s-MIZ.

2.2.5. Sensitivity Analyses

As stated in Auger, Sallée, et al. (2022), the root mean square error between the two-satellite merged product and a third satellite along-track signal is around 3.7 cm. We attempted to test how our results may be sensitive to weak eddies, and in particular to the presence of eddies of amplitude of less than 3.7 cm. As such, we repeated the analysis presented in this paper but removed all eddies that have an amplitude less than 3.7 cm. This sensitivity analysis is shown in Figures S1–S3 of Supporting Information S1. All figures and relationships between sea ice and eddies discussed in this paper remain robust. In order to keep a maximum of eddies in our statistical description of mesoscale eddies, we chose to keep all detected eddies in the remainder of this paper.

Diagnostics derived from eddy identification and tracking may be sensitive to the density of observations, or the position of the satellite tracks before mapping the data set (Amores et al., 2018). To assess the sensitivity of our results to the density of the along-track observations, we repeated the main diagnostics of this paper, but with a data set mapped from subsampled along-track observations. The subsampling method is detailed in Section S1 of Supporting Information S1. The sensitivity test is shown in Figures S1–S3 of Supporting Information S1 as well. The main conclusions presented in this paper remain the same as the original and subsampled data set.

3. Results

3.1. Eddy Kinetic Energy

The spatial distribution of EKE (Figure 2), between the ACC and the Antarctic margins, is strongly influenced by both key circulation features and the sea ice properties of this region. Regions permanently ice-covered are hidden as they are the regions with the highest product errors (Auger, Prandi, & Sallée, 2022). The thick black line in Figure 2 corresponds to the Mean Dynamic Topography contour -180 cm, and is used thereafter as the
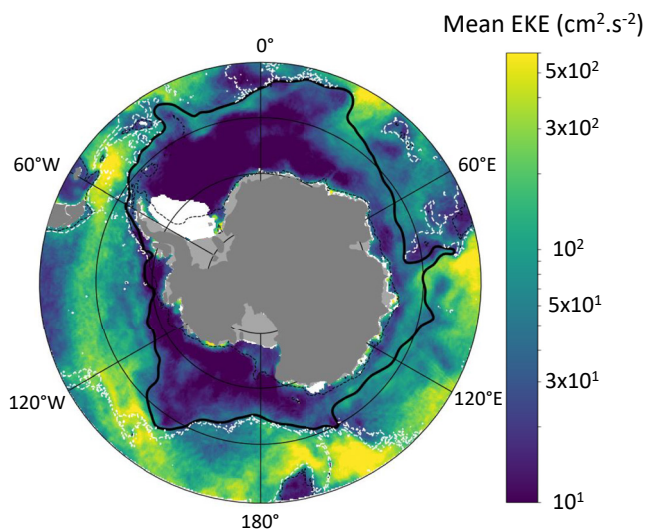
Figure 2. Eddy Kinetic Energy in the Southern Ocean. Eddy Kinetic Energy is computed as $\frac{1}{2}\left(u'^2 + v'^2\right)$, with u' and v' respectively the anomalies of zonal and meridional geostrophic current derived from Auger, Prandi, and Sallée (2022). The colormap used is in logscale. White dashed lines are the $-3,000$ m isobath north of the subpolar Southern Ocean. The black dashed line is the $-1,000$ m isobath. The bold black line is the limit of the subpolar Southern Ocean, defined here as the -180 cm MDT contour from Armitage et al. (2018).

northern extent of the region we refer to as the subpolar Southern Ocean in this paper (Auger, Sallée, et al., 2022). North of this subpolar region, the signature of the ACC is visible with EKE values reaching more than 500 cm^2 s^{-2} in hotspots downstream of the major topographic features, consistent with previous studies (e.g., Y. Zhang et al., 2021). In contrast, the subpolar ocean has a substantially lower level of EKE. Three distinct regions stand out in the seasonally ice-covered region. First, the northern boundary of the subpolar region shows relatively large values of EKE, around 100 cm^2 s^{-2}, which coincides with the southern boundary of the ACC. Second, the regions inside the two main subpolar gyres, the Ross and Weddell gyres, are associated with very low values of EKE of the order of 10 cm^2 s^{-2}. Third, the continental shelf and slope show relatively elevated EKE, but with important disparities depending on sectors around Antarctica. In general, EKE on the continental slope and shelf reaches around several 10's to 100 cm^2 s^{-2}, but reaches several 100 cm^2 s^{-2} in specific regions, such as the Western Amundsen Sea and East Antarctica. These two regions have previously been identified as hosting the most intense Antarctic Slope Current (ASC) in terms of mean flow and variability (Auger, Sallée, et al., 2022). The West Antarctic Peninsula and the Bellingshausen Sea stand out as a region in which peak EKE values are not found at the continental shelf break (black dashed line) but closer to the Antarctic continent (Figure 2). This shift of high EKE values closer to the coast is consistent with the absence of an ASC in this region (Moffat & Meredith, 2018), and with the presence of a strong and variable Antarctic Coastal Current (AACC) (Schubert et al., 2021; Schulze Chretien et al., 2021). When computing monthly EKE maps, one striking signal is a small positive EKE anomaly following the position of the ice edge and the marginal ice zone. Possible explanations for this signal are investigated in Sections 3.3 and 3.4.

We now investigate how this spatial structure in EKE compares to estimates of eddy presence and characteristics. We first describe overall eddy characteristics in the subpolar Southern Ocean, then explore the role of sea ice in modulating eddy occurrence and characteristics, and finally evaluate the difference in eddy characteristics in distinct dynamical regimes of the subpolar region.

3.2. Eddy Detection in the Subpolar Southern Ocean

More than 1.4 million eddy occurrences are found in the detection analysis applied to the 7 years of daily observations. Figure 3 shows three examples of eddies detected in the ice-covered region, which summarizes their position in the sea ice region, the along-track measurements used as inputs of the gridded product, and their signature in the gridded SLA data set. The first row of Figure 3 shows the detection of a cyclonic eddy in the pack ice. The number of measurements within the eddy contour is shown. The eddy represented on the second row (Figures 3d–3f) stands out as an eddy with 725 observations inside its contour. This unusually large number of observation (more observations than 75% of the eddies in lowly concentrated sea ice, Figure S5 in Supporting Information S1) is due to its position close to the ice edge, such that part of the eddy was in the open ocean (denser tracks in the upper part of the panel) where more measurements are available.

While one could expect the regional pattern of EKE and eddy frequency to be similar, their spatial distribution in the subpolar Southern Ocean is different (Figure 4a). Here, we define the eddy detection frequency as the frequency at which a pixel in the data set is within an eddy. The frequency is about 0.2 (meaning that the pixel is detected in an eddy for 20% of the full period of observation) in most of the subpolar Southern Ocean. There is a reduced detection frequency at the continental shelf break and an increase in detection frequency in the gyres. The difference between EKE and eddy detection frequency patterns is, potentially an encouraging indication that EKE patterns are not shaped by the ability of the altimeter product to sample or miss eddies in the subpolar regions. Rather, EKE is shaped by the intensity of the detected eddies (Figure 4b).
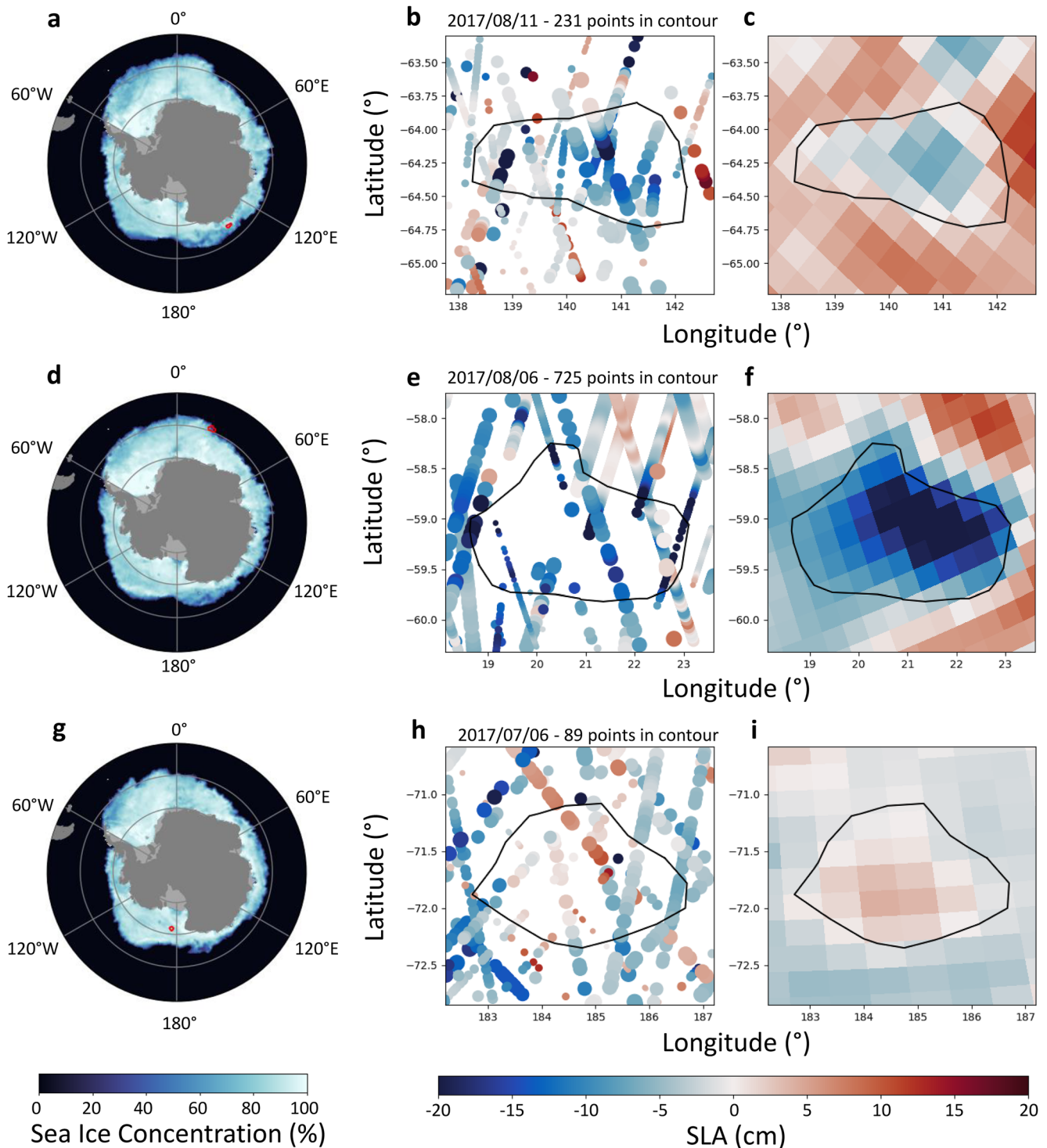
Figure 3. Examples of eddies detected in the sea ice region. Panels (a–c) show a cyclonic eddy in the pack ice, (d–f) show a cyclonic eddy in the marginal ice zone, and (g–j) show an anticyclonic eddy in the pack ice. The first column (a, d, and g) shows the position of the eddy in the Southern Ocean (red contour) and the sea ice concentration. The second column (b, e, and h) shows the along-track measurements from satellite altimetry, and the final contour of the eddy detected. The along-track points show the observations made 7 days before and 7 days after the date of detection. Points closer to the date of detection are wider. The last column (b, e, and h) shows the gridded SLA product and the eddy contour.
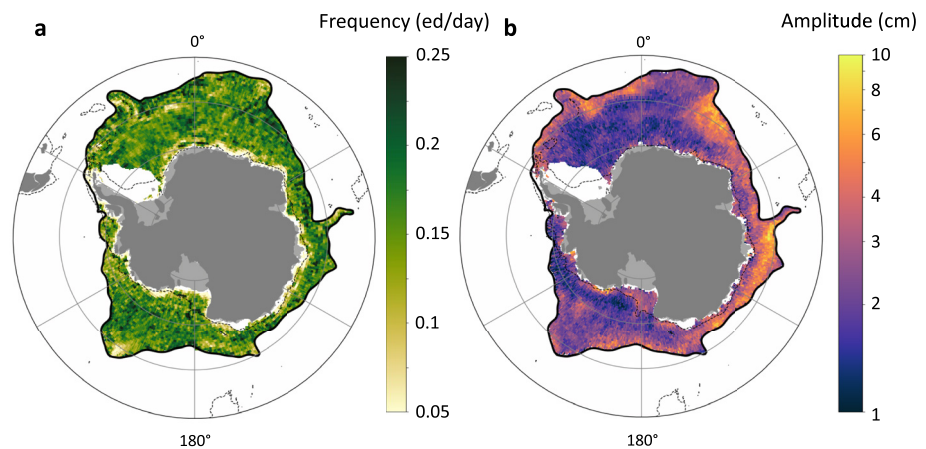
Figure 4. Distribution and amplitude of the detected eddies in the subpolar Southern Ocean. (a) Eddy frequency per pixel in the subpolar Southern Ocean. (b) Mean eddy amplitude per 0.5° pixel in the subpolar Southern Ocean. The black dashed line is the −1,000 m isobath. The bold black line is the limit of the subpolar Southern Ocean as defined in this study.

While the frequency of eddies detected is relatively homogeneous over the subpolar region (Figure 4a), the detected eddies have much weaker amplitudes in the subpolar gyres, compared to the northern or southern boundaries of the subpolar domain (Figure 4b). The amplitude ranges from 5 to 10 cm in the most energetic sectors of the subpolar region, to 1–2 cm in the less energetic regions in the middle of the subpolar gyres. Overall, the spatial patterns of EKE (Figure 2) and of the mean amplitude of the detected eddies (Figure 4b) are similar. This implies that the spatial pattern of EKE is not driven by the frequency of eddy occurrence, but more by the strength of these eddies. While the probability of detecting an eddy is relatively homogeneous over the subpolar ocean domain, the amplitude and the energy associated with these eddies are strongly dependent on the local dynamical regime: southern ACC region, subpolar gyre, and continental shelf break. We next investigate if, on top of the dynamical regime, the seasonal presence or absence of overlying sea ice cover impacts eddy frequency and characteristics.

3.3. Impact of the Sea Ice on Eddy Frequency and Amplitude

The density and amplitude of eddies are very sensitive to SIC, especially for cyclonic eddies (Figure 5). The relationship between the density of eddies and the sea ice concentration is explored by computing the number and surface area of eddies, conditioned by sea ice concentration with 10% bins (Figure 5a). For anticyclones, the density of eddies is roughly constant at around 1.6 anticyclonic eddies per 100,000 km^2. In contrast, the density of cyclonic eddies seems to be more impacted by the overlying sea ice concentration. In the *n*-MIZ, for SIC values between 10% and 40%, the density of cyclonic eddies reaches values up to 2.6 cyclones per 100,000 km^2. Thus, the *n*-MIZ seems to be a favorable region for cyclonic eddies. The density of cyclones is reduced in higher SIC, reaching about 1.6 cyclones per 100,000 km^2 between 60% and 90% of sea ice concentration and is minimum for sea ice concentration of 90%–100% with a density of about 1.4 eddies per 100,000 km^2. In the regions of high SIC (close to 100%), the frequency of detecting cyclones and anticyclones is about the same. The difference in detection frequency between eddy polarity peaks between 10% and 40%.

We could wonder if the variation in the density of eddies as a function of sea ice concentration (fewer eddies with more sea ice) results from scarcer valid sea-level observations in higher sea ice concentrations, which could affect our ability to observe eddies. However, if it was indeed our methodology that was sensitive to the presence of sea ice, it would independently affect observations of cyclones and anticyclones. The robust difference observed here between cyclones and anticyclones is an indication of the robustness of our result that the concentration of sea ice does have an impact on the presence of eddies.

Similar to eddy density, the amplitude of eddies varies with sea ice concentrations (Figure 5b). The shape of the relationship is however slightly different. Eddy amplitude maximizes in regions of lower sea ice concentration, with amplitudes around 3 cm, and minimize in the regions of higher sea ice concentration, with amplitudes around 2 cm. This general tendency is observed for both cyclones and anticyclones, but we find that cyclones are on average 40%–70% larger than anticyclones with a maximum difference in absolute amplitude reaching 1 cm
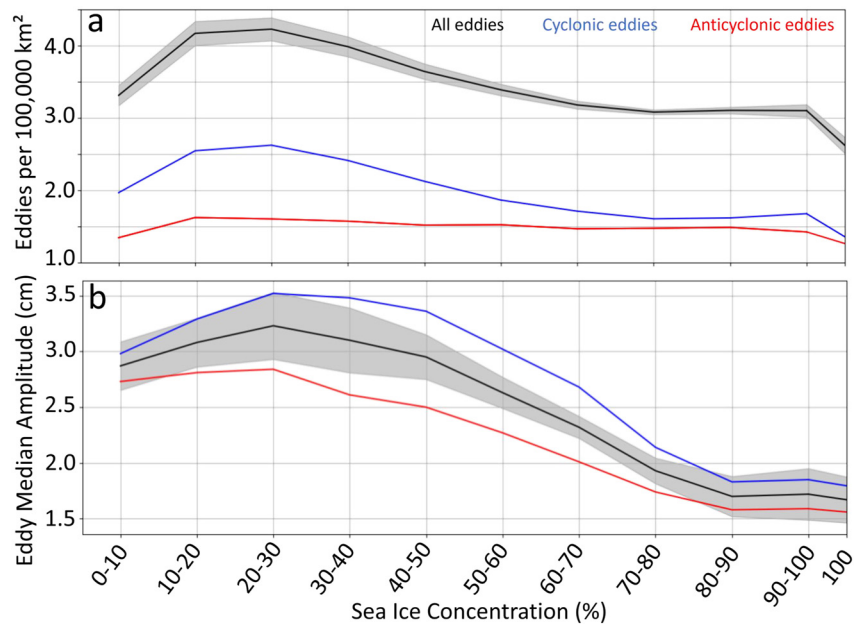
Figure 5. Density and amplitude of the detected eddies as a function of Sea Ice Concentration (SIC). (a) Density of all the eddies (black), cyclonic eddies (blue), and anticyclonic eddies (red) as a function of the sea ice cover. The density is computed as the number of eddies per 100,000 km^2 within each SIC bin. The shaded interval around the density of all the eddies is the standard deviation of this distribution computed for each year of the analysis (2013–2018). (b) Median amplitude of all the eddies (black), cyclonic eddies (blue), and anticyclonic eddies (red) as a function of the sea ice concentration. The shaded interval around the median amplitude of all the eddies is the standard deviation of this distribution computed for each year of the analysis (2013–2018).

in the *n*-MIZ. The amplitude of eddies also strongly varies regionally depending on the local dynamical regime: southern ACC region, gyres, and continental shelf break (Figure 4b). While the proximity to the ACC might be the main driver of the amplitude, further analysis indicates that the impact of sea ice on eddy amplitude differs in the subpolar gyres and at the continental shelf break.

While for all regions of the subpolar Southern Ocean increasing SIC leads to weaker eddies, this effect is stronger in the middle of the gyres and in abyssal plains than at the continental shelf or slope (Figure 6). Figure 6b shows the amplitude of eddies binned as a function of both overlying sea ice concentration bins and underlying bathymetry contours. The associated bathymetry of the subpolar Southern Ocean is shown in Figure 6a. Subpolar gyres are associated with abyssal plains deeper than 3,000–4,000 m, while the continental shelf break is typically associated with bathymetry contours of 500–2,000 m. The overall behavior of larger eddy amplitude in lower sea ice concentration holds for all bathymetry contours. However, there is also a distinct dependence of eddy amplitude on sea-ice concentration in these two sectors: sea ice concentration dampens eddy amplitude more efficiently in abyssal plains compared to the shelf break (Figure 6b). This is illustrated by the ratio between the median eddy amplitudes in the *n*-MIZ (10%–40% SIC) and the pack ice (70%–100% SIC, Figure 6c). This ratio is larger in the deeper water column regions, where the amplitude of the eddies in the *n*-MIZ is twice as high as in the pack ice. The ratio decreases with the depth of the water column, reaching 1.2 over the continental shelf. This is consistent with the presence of an energetic ASC over most of the continental shelf break that might counterbalance eddy dampening by sea ice due to a sustained input of energy from the ASC. We also note that for bathymetry contours corresponding to the continental shelf break, the decrease in eddy amplitude with sea ice concentration stops around 80%, and is followed by an increase for larger sea ice concentration bins. This might result from seasonal variability of the ASC strengths, which substantially increases in winter when sea ice concentration is at its maximum (Armitage et al., 2018; Auger, Sallée, et al., 2022). One could wonder whether the enhanced eddy activity in the *n*-MIZ region could be explained by the proximity of the *n*-MIZ region to the energetic southern ACC. But Figure 6 tells us that this pattern of enhanced eddy activity in the *n*-MIZ region is actually observed in all types of regions of the subpolar Southern Ocean.
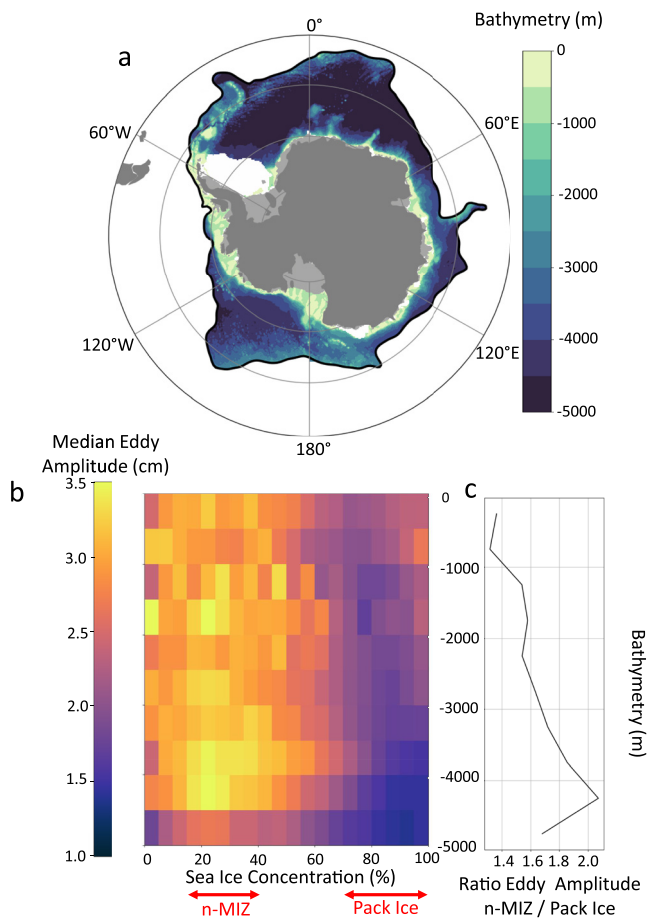
Figure 6. Eddy amplitude as a function of bathymetry and sea ice concentration in the subpolar Southern Ocean. (a) Bathymetry of the subpolar Southern Ocean. (b) Median amplitude of the eddies tracked in the subpolar Southern Ocean as a function of the local bathymetry and the Sea Ice Concentration. Red lines indicate the frontiers of the northern MIZ (*n*-MIZ) and the Pack Ice. (c) Ratio between the median amplitude of the *n*-MIZ and the median amplitude of the pack ice values as a function of bathymetry.

The number of eddies detected in the continental slope region seems to be related to the magnitude of the slope. This is expected as a strong bathymetric slope may be responsible for the suppression of EKE (Isachsen, 2011; Stewart & Thompson, 2013). We find a significant negative correlation between the number of detected eddies and the slope magnitude at the −1,000 isobath, indicating that as the slope magnitude increases, the number of eddies detected decreases. However, the correlation between the number of eddies and the slope magnitude drops to approximately zero for isobaths −1,500 and −2,000, suggesting a weaker or non-existent relationship between these variables at these depths. Although this observation warrants further investigation, it remains beyond the scope of this paper.

3.4. Eddies in the Northern Marginal Ice Zone

The diagnostics presented above that consider the relationship between SIC and the presence and amplitude of eddies indicate that the *n*-MIZ is a unique region. The *n*-MIZ stands out as a region associated with larger eddy density, larger eddy amplitude, and a statistically significant dominance of cyclones over anticyclones. In this section, we investigate some possible reasons for this behavior in the *n*-MIZ. Both Arctic and Antarctic MIZ have been identified as hotspots for eddy-like features in past studies (Lu et al., 2015; Manucharyan & Thompson, 2022) while both mechanical and thermo-dynamical effects have been suggested as potential explanations for these increased instabilities. In the following, we investigate, in turn, if mechanical or thermodynamical forcings would be qualitatively consistent with our results. Eddies in the *n*-MIZ could also propagate from open ocean regions. However, due to the disparity in observational data availability (roughly 10 times more observations in ice-free regions than in ice-covered areas) and spatial resolution (as demonstrated in Figure S4 of Supporting Information S1), comparing eddies in these two regions remains a delicate undertaking. Still, Figure 6 indicates the existence of more intense MIZ eddies, even when the MIZ is situated in the middle of the gyres or in proximity to the continental slope and shelf. This suggests that such phenomena remain relevant, even when further away from the ACC, which is the main candidate for generating eddies in the open Southern Ocean.

In the *n*-MIZ, according to Equation 3, two mechanisms may impact the local surface stress. At the ice edge, the presence of sea ice dampens the transfer of momentum from the winds (wind-ocean stress). Meanwhile, the sea ice velocity and ocean current impact the ice component of the surface stress. Consequently, the *n*-MIZ is a region favorable for a strong horizontal gradient in surface stress, between ice-free, open-ocean regions and partially ice-covered ocean regions. This change in sea ice concentration can lead to strong Ekman pumping velocities (Manucharyan et al., 2022; Ramadhan et al., 2022).

The strong wind-ocean stress in the open ocean and the dampening of the wind-associated surface stress in the ice-covered region may lead to a large stress curl in the *n*-MIZ region. In consequence, the *n*-MIZ is associated with intense upwelling or downwelling, which may create an *n*-MIZ jet favorable for instabilities (Häkkinen, 1986). In the Southern Hemisphere, the strong mid-latitude westerlies, in concert with the sea ice, are efficient at creating strong upwelling at the ice edge and in the *n*-MIZ (Figures 7a and 7b). These Ekman-driven upwellings have the potential to locally increase eddy activity due to both lateral buoyancy gradients and the creation of a local jet following the sea ice edge (Häkkinen, 1986). In summer months, when the sea ice edge is located further south, the easterlies interacting with this local jet may trigger an eddy response as well, as these conditions enhance the formation of intra-pycnocline eddies (Lu et al., 2015; Thomas, 2008). The mechanism of Ekman-driven upwellings and downwellings that favors instabilities is consistent with our observation of a collocated increase in eddy density (Figure 7c) at the *n*-MIZ. On the specific month (June) displayed in Figure 7c, it is striking that
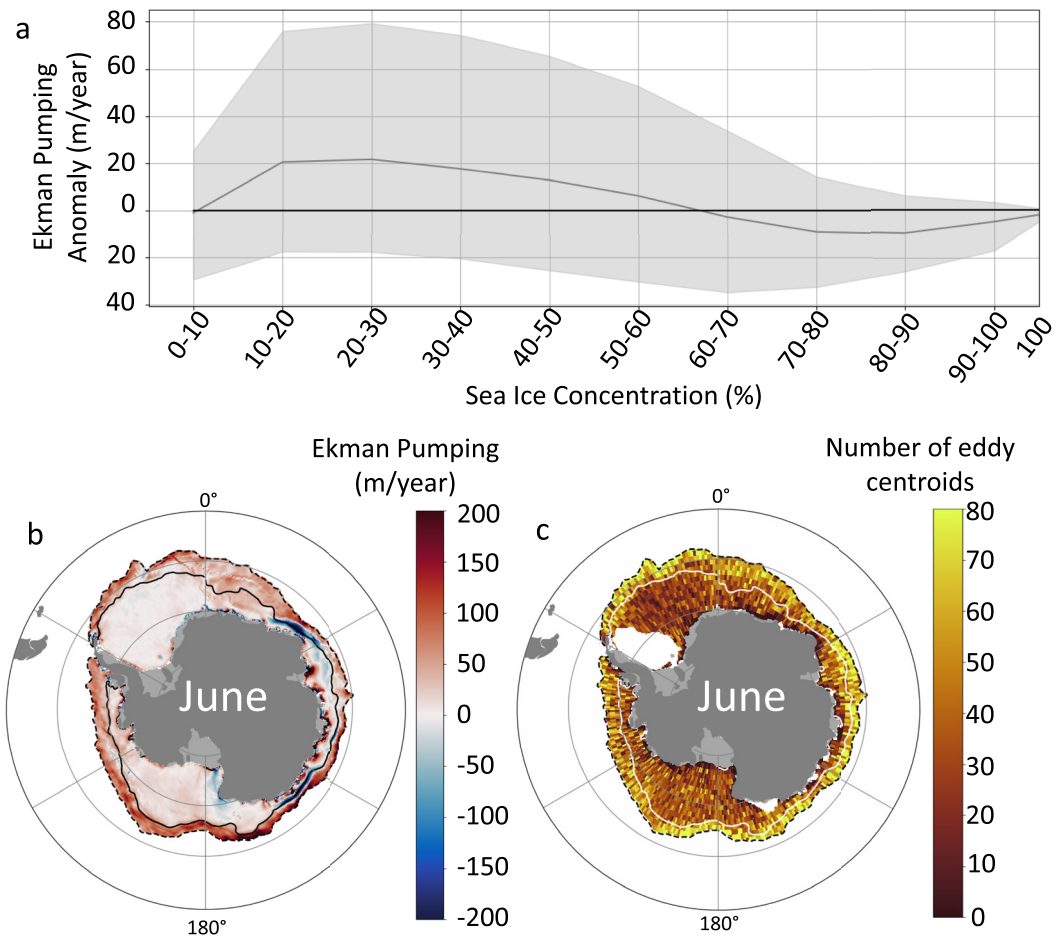
Figure 7. Ekman pumping and number of eddies detected in the ice-covered Southern Ocean. (a) Median Ekman pumping anomaly as a function of sea ice concentration ranges. (b) Mean Ekman pumping velocities in June in the ice-covered region of the Southern Ocean, between 2013 and 2019. (c) Number of eddies detected in 1°pixel in the sea ice zone in June between 2013 and 2019. In (b and c), the dashed, and plain lines are respectively the contours of 10%, and 70% of Sea Ice Concentration.

we detect more eddies in the northern part of the MIZ (Figure 7c), consistent with the location of the largest Ekman-driven upwelling (Figure 7c). The other months show consistent patterns between ocean stress curl and detection hotspots under sea ice.

In addition to mechanical forcing, the *n*-MIZ is also prone to thermodynamical instabilities at the sea ice edge meltwater front (Gupta & Thompson, 2022; Horvat et al., 2016; Lu et al., 2015). Sea ice in the *n*-MIZ provides an important source of freshwater, which when melting, generates a large meridional buoyancy gradient that would enhance instabilities (Lu et al., 2015). In the *n*-MIZ, lateral gradients of density can be found at various scales between 1 and 100 km, which may become unstable and form mixed layer eddies (Giddy et al., 2021; Swart et al., 2020). Here, we tried to link the density and strength of the detected eddies in the *n*-MIZ with seasonal variations in sea ice formation and melt, but found no significant relationship. Hence, we hypothesize that surface stress is the main driver of the presence and strength of enhanced mesoscale activity in the *n*-MIZ. In winter, the *n*-MIZ also coincides with the southern boundary of the ACC. During that period, part of this enhancement could be associated with strong EKE due to the potential energy associated with the strong baroclinic mean flow. However, stronger and more cyclonic eddies are found even when the *n*-MIZ is positioned more south, the ACC cannot be the main driver of these instabilities.

4. Discussion

Our results provide the first, circumpolar assessment of eddy density and properties in ice-covered regions of the Southern Ocean. However, there are important limitations in this data product that we highlight below. First and foremost, the satellite altimetry product (Auger, Prandi, & Sallée, 2022), while being, to our knowledge, the finest resolution SLA product of the subpolar Southern Ocean existing at the time of writing, is gridded at a 25 km resolution, which is larger than the Rossby radius in most of the subpolar ocean. along-track observations are however able to detect smaller-scale signals, as the median number of observations is around 10 observations per gridpoint in the most challenging regions with high SIC (Figure S4 in Supporting Information S1). Furthermore, there are no strong disparities in the number of SSH observations despite varying sea ice concentrations, potentially due to the tightened satellite tracks when going southward compensating for fewer sea ice leads. Many small-scale eddies are necessarily not detected or smoothed out in the altimetry product. Future altimetry missions will fill an important gap in this direction. While it is difficult to assess the impact of such limitations on our results, we did test the robustness of our results to a coarsened observation-based product. Specifically, we repeated the same set of analyses described in Section 3, but from an altimetry data set produced with subsampled along-track observations before mapping to a grid (Section S1 in Supporting Information S1). Both eddy amplitude and eddy density showed a weak sensitivity to the measurement resolution (Figures S1–S3 in Supporting Information S1).

The methodology for detecting and tracking eddies based on satellite-derived sea surface topography has also limitations. For instance, noise in the ocean topography data set may create spurious small eddies. The resolution of the satellite tracks and the optimal interpolation method used for the SLA data set may either miss or create eddies as well (Amores et al., 2018). In particular, Stegner et al. (2021) shows that the irregular satellite sampling and interpolation method could be responsible for the detection of wide cyclonic eddies that would in fact represent several small eddies, or even the detection of spurious eddies. In our study, the asymmetry in the detection of cyclonic eddies, especially in the MIZ, should not be attributed to eddy detection error as the number of observations within the eddies is even higher in the marginal ice zone than in the other regions (Figure S5 in Supporting Information S1). We tested the sensitivity of our result to the possible detection of spurious weak eddies by removing all eddies with amplitudes smaller than an upper bound (3.7 cm) of the evaluated error of the product. This analysis can be found in Figures S1–S3 of Supporting Information S1, and shows that our results are robust to this test.

Our results differ from other studies observing eddies in sea ice-covered regions, as the observation methods and the nature of observations are radically different. Most of the eddies previously observed in the sea ice region have been observed in the halocline, between 50 and 250 m depth, from in situ measurements (Meneghello et al., 2020; Timmermans et al., 2008; Zhao et al., 2014, 2016). Those eddies are mostly anticyclonic (Zhao et al., 2014, 2016), and are unlikely to be impacted by the overlying sea ice as they may have lifetimes lasting more than 6 months (Timmermans et al., 2008). Here, we observe a dominance of cyclonic eddies over anticyclonic eddies in both the ice-free and ice-covered subpolar Southern Ocean. Except close to the main features of the background circulation such as the ACC or ASC, eddies seem to be sensitive to the presence of sea ice. This is consistent with the winter dampening of surface eddy kinetic energy that was discussed in the Arctic by Meneghello et al. (2020). However, this dampening should be weaker in the Southern Ocean due to thinner sea ice. Our results show that the northern part of the MIZ is a region favorable for eddies, particularly cyclones. Multiple studies have demonstrated the MIZ to be a region with an intense eddy activity, due to its meltwater fronts (Giddy et al., 2021; Horvat et al., 2016; Lu et al., 2015) or the local wind-driven upwellings or downwelling at the ice edge (Häkkinen, 1986) and subsequent jet (Thomas, 2008). The dominance of cyclonic eddies in this study may in fact reflect the structure of the eddies in the MIZ. Taking inspiration from the fronts at Arctic sea ice edges, Manucharyan and Timmermans (2013) demonstrated that eddies generated at surface fronts are often formed as dipoles, with surface cyclones and weaker subsurface anticyclones. Those anticyclones then travel in the halocline of the sub-ice regions far from their formation regions (Manucharyan & Timmermans, 2013; Timmermans et al., 2008) where they have been observed by multiple studies (Timmermans et al., 2008; Z. Zhang et al., 2014; Zhao et al., 2016). Consequently, the observed dominance of cyclones in the n-MIZ may be the surface signature of the generation of halocline anticyclones. While the eddy generation mechanism is an interesting area to pursue in future studies, this data set demonstrates that intense eddy generation likely occurs at the sea ice edge.

5. Conclusion

We have used a new satellite altimetry product, covering both the ice-free and ice-covered Southern Ocean to investigate eddy activity in the subpolar sector of the Southern Ocean, to document the spatial distribution of EKE, the number of eddies per unit area, and eddy amplitudes. The data set indicates that sea ice cover provides a key control over eddy properties. The spatial distribution of EKE is consistent with the location of the main circulation features of the Southern Ocean. Enhanced EKE is found in the ACC downstream of the major topographic features, and more generally follows the path of the ACC and ASC. These regions are also associated with larger amplitude coherent eddies. With higher SIC, the number of eddies observed per unit area as well as their amplitude decreases. While there is the potential that these results reflect a methodological bias, in which the presence of sea ice reduces the number of valid observations within a given pixel and therefore the ability to detect eddies, a number of different sensitivity tests suggest that the results are robust. For example, a methodological bias would likely impact then detection of cyclones and anticyclones in a similar manner. Yet, the data set reveals that sea ice cover mostly affects cyclones, with the *n*-MIZ being a hotspot of strong cyclonic eddies. The higher cyclonic eddy density and strength in the *n*-MIZ compared to the pack ice is enhanced in the middle of the gyres, where the background circulation should only allow weak eddy generation, in contrast with the south-ACC or ASC regions. In the *n*-MIZ, both freshwater fluxes from sea ice melt and sea ice edge-driven upwelling through Ekman pumping may contribute to frontogenesis that would intensify the eddy growth and eddy activity. We find that Ekman pumping could be one of the main driver for these *n*-MIZ instabilities, as the region is impacted by strong surface stress curl anomalies all around Antarctica and the meridional position is consistent with enhanced detection of mesoscale eddies.

Data Availability Statement

The Sea Level Anomaly data used in this study are available at Auger et al. (2021) via the https://doi.org/10.17882/81032 and described in Auger, Prandi, and Sallée (2022).

References

Amores, A., Jordà, G., Arsouze, T., & Sommer, J. L. (2018). Up to what extent can we characterize ocean eddies using present-day gridded altimetric products? *Journal of Geophysical Research: Oceans*, *123*(10), 7220–7236. https://doi.org/10.1029/2018JC014140

Armitage, T. W. K., Kwok, R., Thompson, A. F., & Cunningham, G. (2018). Dynamic topography and sea level anomalies of the Southern Ocean: Variability and teleconnections. *Journal of Geophysical Research: Oceans*, *123*(1), 613–630. https://doi.org/10.1002/2017JC013534

Auger, M., Prandi, P., & Sallée, J.-B. (2021). Daily Southern Ocean sea level anomaly and geostrophic currents from multimission altimetry, 2013–2019 [Dataset]. SEANOE. https://doi.org/10.17882/81032

Auger, M., Prandi, P., & Sallée, J.-B. (2022). Southern ocean sea level anomaly in the sea ice-covered sector from multimission satellite observations. *Scientific Data*, *9*(1), 70. https://doi.org/10.1038/s41597-022-01166-z

Auger, M., Sallée, J.-B., Prandi, P., & Naveira Garabato, A. C. (2022). Subpolar Southern Ocean seasonal variability of the geostrophic circulation from multi-mission satellite altimetry. *Journal of Geophysical Research: Oceans*, *127*(6), e2021JC018096. https://doi.org/10.1029/2021JC018096

Bishop, S. P., Gent, P. R., Bryan, F. O., Thompson, A. F., Long, M. C., & Abernathey, R. (2016). Southern Ocean overturning compensation in an eddy-resolving climate simulation. *Journal of Physical Oceanography*, *46*(5), 1575–1592. https://doi.org/10.1175/JPO-D-15-0177.1

Brodzik, M. J., Billingsley, B., Haran, T., Raup, B., & Savoie, M. H. (2014). Correction: Brodzik, M. J., et al. EASE-Grid 2.0: Incremental but Significant Improvements for Earth-Gridded Data Sets. ISPRS International Journal of Geo-Information 2012, 1, 32–45. *ISPRS International Journal of Geo-Information*, *3*(3), 1154–1156. https://doi.org/10.3390/ijgi3031154

Chelton, D. B. (2013). Mesoscale eddy effects. *Nature Geoscience*, *6*(8), 594–595. https://doi.org/10.1038/ngeo1906

Chelton, D. B., de Szoeke, R. A., Schlax, M. G., Naggar, K. E., & Siwertz, N. (1998). Geographical variability of the first baroclinic Rossby radius of deformation. *Journal of Physical Oceanography*, *28*(3), 433–460. https://doi.org/10.1175/1520-0485(1998)028⟨0433:GVOTFB⟩2.0.CO;2

Chelton, D. B., Schlax, M. G., & Samelson, R. M. (2011). Global observations of nonlinear mesoscale eddies. *Progress in Oceanography*, *91*(2), 167–216. https://doi.org/10.1016/j.pocean.2011.01.002

Ducet, N., Traon, P. Y. L., & Reverdin, G. (2000). Global high-resolution mapping of ocean circulation from TOPEX/Poseidon and ERS-1 and -2. *Journal of Geophysical Research*, *105*(C8), 19477–19498. https://doi.org/10.1029/2000JC900063

Dufour, C. O., Sommer, J. L., Zika, J. D., Gehlen, M., Orr, J. C., Mathiot, P., & Barnier, B. (2012). Standing and transient eddies in the response of the Southern Ocean meridional overturning to the southern annular mode. *Journal of Climate*, *25*(20), 6958–6974. https://doi.org/10.1175/JCLI-D-11-00309.1

Escudier, R., Renault, L., Pascual, A., Brasseur, P., Chelton, D., & Beuvier, J. (2016). Eddy properties in the Western Mediterranean Sea from satellite altimetry and a numerical simulation. *Journal of Geophysical Research: Oceans*, *121*(6), 3990–4006. https://doi.org/10.1002/2015JC011371

Farneti, R., Delworth, T. L., Rosati, A. J., Griffies, S. M., & Zeng, F. (2010). The role of mesoscale eddies in the rectification of the Southern Ocean response to climate change. *Journal of Physical Oceanography*, *40*(7), 1539–1557. https://doi.org/10.1175/2010JPO4353.1

Garabato, A. C. N., Dotto, T. S., Hooley, J., Bacon, S., Tsamados, M., Ridout, A., et al. (2019). Phased response of the subpolar Southern Ocean to changes in circumpolar winds. *Geophysical Research Letters*, *46*(11), 6024–6033. https://doi.org/10.1029/2019GL082850

Garrett, C. (1983). On the initial streakness of a dispersing tracer in two- and three-dimensional turbulence. *Dynamics of Atmospheres and Oceans*, *7*(4), 265–277. https://doi.org/10.1016/0377-0265(83)90008-8

Gent, P. R. (2016). Effects of Southern Hemisphere wind changes on the meridional overturning circulation in ocean models. *Annual Review of Marine Science*, *8*(1), 79–94. https://doi.org/10.1146/annurev-marine-122414-033929

Gent, P. R., Willebrand, J., McDougall, T. J., & McWilliams, J. C. (1995). Parameterizing eddy-induced tracer transports in ocean circulation models. *Journal of Physical Oceanography*, *25*(4), 463–474. https://doi.org/10.1175/1520-0485(1995)025⟨0463:PEITTI⟩2.0.CO;2

Giddy, I., Swart, S., du Plessis, M., Thompson, A. F., & Nicholson, S.-A. (2021). Stirring of sea-ice meltwater enhances submesoscale fronts in the Southern Ocean. *Journal of Geophysical Research: Oceans*, *126*(4), e2020JC016814. https://doi.org/10.1029/2020JC016814

Gille, S. T. (1997). The Southern Ocean momentum balance: Evidence for topographic effects from numerical model output and altimeter data. *Journal of Physical Oceanography*, *27*(10), 2219–2232. https://doi.org/10.1175/1520-0485(1997)027⟨2219:TSOMBE⟩2.0.CO;2

Gupta, M., & Thompson, A. F. (2022). Regimes of sea-ice floe melt: Ice-ocean coupling at the submesoscales. *Journal of Geophysical Research: Oceans*, *127*(9), e2022JC018894. https://doi.org/10.1029/2022JC018894

Häkkinen, S. (1986). Coupled ice-ocean dynamics in the marginal ice zones: Upwelling/downwelling and eddy generation. *Journal of Geophysical Research*, *91*(C1), 819–832. https://doi.org/10.1029/JC091iC01p00819

Horvat, C., Tziperman, E., & Campin, J.-M. (2016). Interaction of sea ice floe size, ocean eddies, and sea ice melting. *Geophysical Research Letters*, *43*(15), 8083–8090. https://doi.org/10.1002/2016GL069742

Ice, J. E. T. o. S. (2009). WMO Sea-ice Nomenclature, WMO/OMM/BMO - No. 259 Suppl. No. 5. Linguistic equivalents. https://doi.org/10.25607/OBP-1530

Isachsen, P. E. (2011). Baroclinic instability and eddy tracer transport across sloping bottom topography: How well does a modified Eady model do in primitive equation simulations? *Ocean Modelling*, *39*(1), 183–199. https://doi.org/10.1016/j.ocemod.2010.09.007

Ivchenko, V. O., Danilov, S., & Olbers, D. (2008). Eddies in numerical models of the Southern Ocean. In *Ocean modeling in an eddying regime* (pp. 177–198). American Geophysical Union (AGU). https://doi.org/10.1029/177GM13

Jayne, S. R., & Marotzke, J. (2002). The oceanic eddy heat transport. *Journal of Physical Oceanography*, *32*(12), 3328–3345. https://doi.org/10.1175/1520-0485(2002)032⟨3328:TOEHT⟩2.0.CO;2

Kozlov, I. E., Artamonova, A. V., Manucharyan, G. E., & Kubryakov, A. A. (2019). Eddies in the Western Arctic Ocean from spaceborne SAR observations over open ocean and marginal ice zones. *Journal of Geophysical Research: Oceans*, *124*(9), 6601–6616. https://doi.org/10.1029/2019JC015113

Kubryakov, A. A., Kozlov, I. E., & Manucharyan, G. E. (2021). Large mesoscale eddies in the Western Arctic Ocean from satellite altimetry measurements. *Journal of Geophysical Research: Oceans*, *126*(5), e2020JC016670. https://doi.org/10.1029/2020JC016670

Larichev, V. D., & Held, I. M. (1995). Eddy amplitudes and fluxes in a homogeneous model of fully developed baroclinic instability. *Journal of Physical Oceanography*, *25*(10), 2285–2297. https://doi.org/10.1175/1520-0485(1995)025⟨2285:EAAFIA⟩2.0.CO;2

Lu, K., Weingartner, T., Danielson, S., Winsor, P., Dobbins, E., Martini, K., & Statscewich, H. (2015). Lateral mixing across ice meltwater fronts of the Chukchi Sea shelf. *Geophysical Research Letters*, *42*(16), 6754–6761. https://doi.org/10.1002/2015GL064967

Manucharyan, G. E., Lopez-Acosta, R., & Wilhelmus, M. M. (2022). Spinning ice floes reveal intensification of mesoscale eddies in the western Arctic Ocean. *Scientific Reports*, *12*(1), 7070. https://doi.org/10.1038/s41598-022-10712-z

Manucharyan, G. E., & Thompson, A. F. (2022). Heavy footprints of upper-ocean eddies on weakened Arctic sea ice in marginal ice zones. *Nature Communications*, *13*(1), 2147. https://doi.org/10.1038/s41467-022-29663-0

Manucharyan, G. E., & Timmermans, M.-L. (2013). Generation and separation of mesoscale eddies from surface ocean fronts. *Journal of Physical Oceanography*, *43*(12), 2545–2562. https://doi.org/10.1175/JPO-D-13-094.1

Marshall, G. J. (2003). Trends in the Southern Annular Mode from observations and reanalyses. *Journal of Climate*, *16*(24), 4134–4143. https://doi.org/10.1175/1520-0442(2003)016⟨4134:TITSAM⟩2.0.CO;2

Marshall, J., & Radko, T. (2003). Residual-mean solutions for the Antarctic Circumpolar Current and its associated overturning circulation. *Journal of Physical Oceanography*, *33*(11), 2341–2354. https://doi.org/10.1175/1520-0485(2003)033⟨2341:RSFTAC⟩2.0.CO;2

Martin, T., Tsamados, M., Schroeder, D., & Feltham, D. L. (2016). The impact of variable sea ice roughness on changes in Arctic Ocean surface stress: A model study. *Journal of Geophysical Research: Oceans*, *121*(3), 1931–1952. https://doi.org/10.1002/2015JC011186

Mason, E., Pascual, A., & McWilliams, J. C. (2014). A new sea surface height–based code for oceanic mesoscale eddy tracking. *Journal of Atmospheric and Oceanic Technology*, *31*(5), 1181–1188. https://doi.org/10.1175/JTECH-D-14-00019.1

McWilliams, J. C. (1985). Submesoscale, coherent vortices in the ocean. *Reviews of Geophysics*, *23*(2), 165–182. https://doi.org/10.1029/RG023i002p00165

Meier, W. N., Fetterer, F., Savoie, M., Mallory, S., Duerr, R., & Stroeve, J. (2017). NOAA/NSIDC climate data record of passive microwave sea ice concentration, version 3 [Dataset]. NSIDC. https://doi.org/10.7265/N59P2ZTG

Meneghello, G., Marshall, J., Lique, C., Isachsen, P. E., Doddridge, E., Campin, J.-M., et al. (2020). Genesis and decay of mesoscale baroclinic eddies in the seasonally ice-covered interior Arctic Ocean. *Journal of Physical Oceanography*, *51*(1), 115–129. https://doi.org/10.1175/JPO-D-20-0054.1

Moffat, C., & Meredith, M. (2018). Shelf-ocean exchange and hydrography west of the Antarctic Peninsula: A review. *Philosophical Transactions. Series A, Mathematical, Physical, and Engineering Sciences*, *376*(2122), 20170164. https://doi.org/10.1098/rsta.2017.0164

Morrow, R., & Le Traon, P.-Y. (2012). Recent advances in observing mesoscale ocean dynamics with satellite altimetry. *Advances in Space Research*, *50*(8), 1062–1076. https://doi.org/10.1016/j.asr.2011.09.033

Nakayama, Y., Ohshima, K. I., Matsumura, Y., Fukamachi, Y., & Hasumi, H. (2014). A numerical investigation of formation and variability of Antarctic Bottom Water off Cape Darnley, East Antarctica. *Journal of Physical Oceanography*, *44*(11), 2921–2937. https://doi.org/10.1175/JPO-D-14-0069.1

Nøst, O. A., Biuw, M., Tverberg, V., Lydersen, C., Hattermann, T., Zhou, Q., et al. (2011). Eddy overturning of the Antarctic Slope Front controls glacial melting in the Eastern Weddell Sea. *Journal of Geophysical Research*, *116*(C11), C11014. https://doi.org/10.1029/2011JC006965

Palóczy, A., Gille, S. T., & McClean, J. L. (2018). Oceanic heat delivery to the Antarctic continental shelf: Large-scale, low-frequency variability. *Journal of Geophysical Research: Oceans*, *123*(11), 7678–7701. https://doi.org/10.1029/2018JC014345

Patara, L., Böning, C. W., & Biastoch, A. (2016). Variability and trends in Southern Ocean eddy activity in 1/12° ocean model simulations. *Geophysical Research Letters*, *43*(9), 4517–4523. https://doi.org/10.1002/2016GL069026

Pegliasco, C., Delepoulle, A., Morrow, R., Faugère, Y., & Dibarboure, G. (2021). META3.1exp: A new global mesoscale eddy trajectories atlas derived from altimetry. *Earth System Science Data Discussions*, 1–31. https://doi.org/10.5194/essd-2021-300

Peng, G., Meier, W. N., Scott, D. J., & Savoie, M. H. (2013). A long-term and reproducible passive microwave sea ice concentration data record for climate studies and monitoring. *Earth System Science Data*, *5*(2), 311–318. https://doi.org/10.5194/essd-5-311-2013

Ramadhan, A., Marshall, J., Meneghello, G., Illari, L., & Speer, K. (2022). Observations of upwelling and downwelling around Antarctica mediated by sea ice. *Frontiers in Marine Science*, *9*. https://doi.org/10.3389/fmars.2022.864808

Rintoul, S., Hughes, C., & Olbers, D. (2001). The Antarctic circumpolar current system. *International Geophysics*, *77*, 271. https://doi.org/10.1016/S0074-6142(01)80124-8

Rintoul, S. R. (2018). The global influence of localized dynamics in the Southern Ocean. *Nature*, *558*(7709), 209–218. https://doi.org/10.1038/s41586-018-0182-3

Schaffer, J., Timmermann, R., Arndt, J. E., Rosier, S. H. R., Anker, P. G. D., Callard, S. L., et al. (2019). An update to Greenland and Antarctic ice sheet topography, cavity geometry, and global bathymetry (RTopo-2.0.4). Supplement to: Schaffer, Janin; Kanzow, Torsten; von Appen, Wilken-Jon; von Albedyll, Luisa; Arndt, Jan Erik; Roberts, David H (2020): Bathymetry constrains ocean heat supply to Greenland's largest glacier tongue. *Nature Geoscience*, *13*(3), 227–231. https://doi.org/10.1594/PANGAEA.905295

Schubert, R., Thompson, A., Speer, K., Chretien, L., & Bebieva, Y. (2021). The Antarctic coastal current in the Bellingshausen Sea. *The Cryosphere*, *15*(9), 4179–4199. https://doi.org/10.5194/tc-15-4179-2021

Schulze Chretien, L. M., Thompson, A. F., Flexas, M. M., Speer, K., Swaim, N., Oelerich, R., et al. (2021). The shelf circulation of the Bellingshausen Sea. *Journal of Geophysical Research: Oceans*, *126*(5), e2020JC016871. https://doi.org/10.1029/2020JC016871

Sévigny, C., Gratton, Y., & Galbraith, P. S. (2015). Frontal structures associated with coastal upwelling and ice-edge subduction events in southern Beaufort Sea during the Canadian Arctic Shelf Exchange Study. *Journal of Geophysical Research: Oceans*, *120*(4), 2523–2539. https://doi.org/10.1002/2014JC010641

Speer, K., Rintoul, S. R., & Sloyan, B. (2000). The diabatic Deacon cell. *Journal of Physical Oceanography*, *30*(12), 3212–3222. https://doi.org/10.1175/1520-0485(2000)030⟨3212:TDDC⟩2.0.CO;2

Stammer, D. (1998). On eddy characteristics, eddy transports, and mean flow properties. *Journal of Physical Oceanography*, *28*(4), 727–739. https://doi.org/10.1175/1520-0485(1998)028⟨0727:OECETA⟩2.0.CO;2

Stegner, A., Le Vu, B., Dumas, F., Ghannami, M. A. A., Nicolle, A., Durand, C., & Faugere, Y. (2021). Cyclone-anticyclone asymmetry of eddy detection on gridded altimetry product in the Mediterranean Sea. *Journal of Geophysical Research: Oceans*, *126*(9). https://doi.org/10.1029/2021JC017475

Stewart, A. L., Klocker, A., & Menemenlis, D. (2018). Circum-Antarctic shoreward heat transport derived from an eddy- and tide-resolving simulation. *Geophysical Research Letters*, *45*(2), 834–845. https://doi.org/10.1002/2017GL075677

Stewart, A. L., Klocker, A., & Menemenlis, D. (2019). Acceleration and overturning of the Antarctic slope current by winds, eddies, and tides. *Journal of Physical Oceanography*, *49*(8), 2043–2074. https://doi.org/10.1175/JPO-D-18-0221.1

Stewart, A. L., & Thompson, A. F. (2013). Connecting Antarctic cross-slope exchange with Southern Ocean overturning. *Journal of Physical Oceanography*, *43*(7), 1453–1471. https://doi.org/10.1175/JPO-D-12-0205.1

Stewart, A. L., & Thompson, A. F. (2015). Eddy-mediated transport of warm Circumpolar Deep Water across the Antarctic shelf break. *Geophysical Research Letters*, *42*(2), 432–440. https://doi.org/10.1002/2014GL062281

Swart, S., du Plessis, M. D., Thompson, A. F., Biddle, L. C., Giddy, I., Linders, T., et al. (2020). Submesoscale fronts in the Antarctic marginal ice zone and their response to wind forcing. *Geophysical Research Letters*, *47*(6), e2019GL086649. https://doi.org/10.1029/2019GL086649

Taburet, G., Sanchez-Roman, A., Ballarotta, M., Pujol, M.-I., Legeais, J.-F., Fournier, F., et al. (2019). DUACS DT2018: 25 years of reprocessed sea level altimetry products. *Ocean Science*, *15*(5), 1207–1224. https://doi.org/10.5194/os-15-1207-2019

Thomas, L. N. (2008). Formation of intrathermocline eddies at ocean fronts by wind-driven destruction of potential vorticity. *Dynamics of Atmospheres and Oceans*, *45*(3), 252–273. https://doi.org/10.1016/j.dynatmoce.2008.02.002

Thompson, A. F., Heywood, K. J., Schmidtko, S., & Stewart, A. L. (2014). Eddy transport as a key component of the Antarctic overturning circulation. *Nature Geoscience*, *7*(12), 879–884. https://doi.org/10.1038/ngeo2289

Timmermans, M.-L., Toole, J., Proshutinsky, A., Krishfield, R., & Plueddemann, A. (2008). Eddies in the Canada Basin, Arctic Ocean, observed from ice-tethered profilers. *Journal of Physical Oceanography*, *38*(1), 133–145. https://doi.org/10.1175/2007JPO3782.1

Tsamados, M., Feltham, D. L., Schroeder, D., Flocco, D., Farrell, S. L., Kurtz, N., et al. (2014). Impact of variable atmospheric and oceanic form drag on simulations of Arctic sea ice. *Journal of Physical Oceanography*, *44*(5), 1329–1353. https://doi.org/10.1175/JPO-D-13-0215.1

Tschudi, M., Fowler, C., Maslanik, J., Stewart, J. S., & Meier, W. N. (2016). Polar Pathfinder Daily 25 km EASE-Grid Sea Ice Motion Vectors, Version 3 [Dataset]. NASA National Snow and Ice Data Center DAAC. https://doi.org/10.5067/O57VAIT2AYYY

Vernet, M., Geibert, W., Hoppema, M., Brown, P. J., Haas, C., Hellmer, H. H., et al. (2019). The Weddell Gyre, Southern Ocean: Present knowledge and future challenges. *Reviews of Geophysics*, *57*(3), 623–708. https://doi.org/10.1029/2018RG000604

Visbeck, M., Marshall, J., Haine, T., & Spall, M. (1997). Specification of eddy transfer coefficients in coarse-resolution ocean circulation models. *Journal of Physical Oceanography*, *27*(3), 381–402. https://doi.org/10.1175/1520-0485(1997)027⟨0381:SOETCI⟩2.0.CO;2

Watanabe, E. (2011). Beaufort shelf break eddies and shelf-basin exchange of Pacific summer water in the western Arctic Ocean detected by satellite and modeling analyses. *Journal of Geophysical Research*, *116*(C8), C08034. https://doi.org/10.1029/2010JC006259

Zhang, Y., Chambers, D., & Liang, X. (2021). Regional trends in Southern Ocean eddy kinetic energy. *Journal of Geophysical Research: Oceans*, *126*(6), e2020JC016973. https://doi.org/10.1029/2020JC016973

Zhang, Z., Wang, W., & Qiu, B. (2014). Oceanic mass transport by mesoscale eddies. *Science*, *345*(6194), 322–324. https://doi.org/10.1126/science.1252418

Zhao, M., Timmermans, M.-L., Cole, S., Krishfield, R., Proshutinsky, A., & Toole, J. (2014). Characterizing the eddy field in the Arctic Ocean halocline. *Journal of Geophysical Research: Oceans*, *119*(12), 8800–8817. https://doi.org/10.1002/2014JC010488

Zhao, M., Timmermans, M.-L., Cole, S., Krishfield, R., & Toole, J. (2016). Evolution of the eddy field in the Arctic Ocean's Canada Basin, 2005–2015. *Geophysical Research Letters*, *43*(15), 8106–8114. https://doi.org/10.1002/2016GL069671